Flexible manipulation of optical angular momentum using spherical wavefront supplement

SHUAICHAO LI,[1] HONGJIE HUANG,[1] YILI LU,[1]PEI WANG,[1,2] AND YONGHUA LU[1,2,*]

[1]*Department of Optics and Optical Engineering, University of Science and Technology of China, Hefei 230026, China*

[2]*Advanced Laser Technology Laboratory of Anhui Province, Hefei, Anhui 230026, China*

**Corresponding author: yhlu@ustc.edu.cn*

Table of Contents

S1、Mathematical description of the scattered light

S1.1 Generation of circularly polarized light

Circularly polarized light can be generated by combining two mutually orthogonal polarization components with appropriate phase difference. In previous work, it has been proven that the scattered light from a rectangular metal aperture is equivalent to the radiation from a radiating dipole[1]. Therefore, by arranging two orthogonal apertures and introducing appropriate phase difference, circularly polarized scattered light with specific handedness can be generated.

To describe this phenomenon mathematically, we use the Jones vector $|E\rangle = \boldsymbol{A}e^{i\delta}$ to describe the polarization and phase state of light, and a 2×2 Jones matrix $J = \begin{pmatrix} \tilde{t}_l & 0 \\ 0 & \tilde{t}_w \end{pmatrix}$ to describe the transmission response of the aperture, where $\tilde{t}_l$ and $\tilde{t}_w$ are the complex transmittance of incident light along the long and wide axis of the aperture, respectively. The geometrical parameters of the apertures are shown in Fig.S1(a), where two paired apertures are orthogonally arranged, aperture 1 rotates around the z axis at an angle of θ and aperture 2 rotates around the z axis at an angle of $(\theta + \pi/2)$. When light is incident on these apertures, the scattered light can be expressed as[2]:

$$|E_{scat}\rangle = R(-\theta)\begin{pmatrix} \tilde{t}_l & 0 \\ 0 & \tilde{t}_w \end{pmatrix} R(\theta)|E_{in1}\rangle + R(-(\theta+\pi/2))\begin{pmatrix} \tilde{t}_l & 0 \\ 0 & \tilde{t}_w \end{pmatrix} R(\theta+\pi/2)|E_{in2}\rangle, \tag{S1}$$

where the rotation matrix $R(\theta) = \begin{pmatrix} \cos\theta & \sin\theta \\ -\sin\theta & \cos\theta \end{pmatrix}$. Thus, the polarization state of the scattered light depends on the complex transmittance of the aperture. Using finite-difference time-domain (FDTD) simulations, we computed the transmittance for a single aperture with parameters of $l = 150nm$ and $w = 60nm$ under different wavelengths light incidence, the results are shown in Fig.S1(b) and Fig.S1(c), the transmittance along short axis of the aperture is much stronger than that of long axis (at order of 10^3). Therefore, the scattering field from one aperture can be treated as a dipole oriented along the short axis of the aperture. Furthermore, for this paired apertures, if the incident light is polarized along x direction where $\boldsymbol{A}_{in1} = \boldsymbol{A}_{in2} = \begin{pmatrix} 1 \\ 0 \end{pmatrix}$, and the rotation angle is $\theta = \pi/4$, the scattered light can be simplified as:

$$|E_{scat}\rangle = \frac{\tilde{t}_w}{2}\left(\begin{bmatrix} 1 \\ -1 \end{bmatrix} e^{i\delta_1} + \begin{bmatrix} 1 \\ 1 \end{bmatrix} e^{i\delta_2}\right), \tag{S2}$$

Under this circumstance, the circular polarization state of the scattered light is directly related to the initial phase difference $\Delta\delta = \delta_2 - \delta_1$ between the two apertures, which is dependent on the incident light.

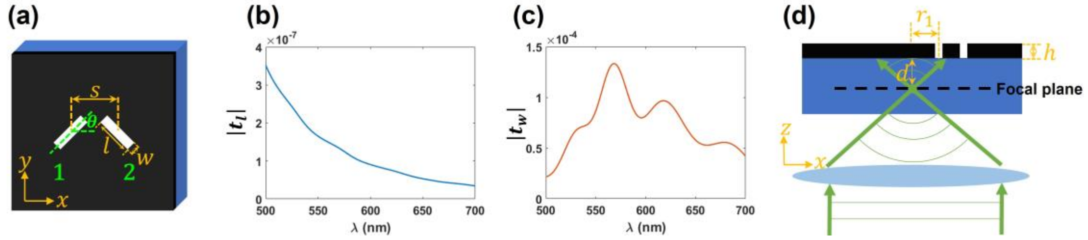

Fig.S1: (a) Schematic view of the Λ-shaped apertures. (b)Transmittance along the long axis at parameters $l = 150nm, w = 60nm$. (c) Transmittance along the short axis at parameters $l = 150nm$ and $w = 60nm$. (d) Schematic showing the phase difference introduced at defocus position where d>0.

For spherical wave incidence, the phase of the wave varies at each point on the spherical surface, hence by arranging those apertures at appropriate lateral distance relative to the beam center will introduce the desired phase difference. Specifically, a lens transformed spherical wave can be expressed as[3]:

$$|E_{in}\rangle = \boldsymbol{A}_{in} e^{i\delta} = \boldsymbol{A}_{in} e^{i\frac{n_g \pi}{d\lambda} r^2}, \tag{S3}$$

where d is the vertical defocus distance of the structure with relative to the focal point of the lens. ($d>0$ diverging spherical wave incidence, $d<0$ converging spherical wave incidence), r is the lateral distance from the beam center, n_g is the refractive index of the medium in the incident side of light. λ is the free-space wavelength of the incident light. A more intuitive schematic diagram of the principle is shown in Fig.S1(d). If aperture 1's lateral distance r_1 and the spacing $s = r_2 - r_1$ between those apertures are set to be:

$$s = \sqrt{r_1^2 + \frac{|d|\lambda}{2n_g}} - r_1, \tag{S4}$$

the phase difference between the two apertures is introduced as:

$$\Delta\delta = \delta_2 - \delta_1 = \begin{cases} \dfrac{\pi}{2} & d > 0 \\ -\dfrac{\pi}{2} & d < 0 \end{cases}, \tag{S5}$$

and the scattered light from the paired apertures are assigned with specific circular polarization states:

$$\left|E_{scat}\right\rangle = \begin{cases} \dfrac{(1+i)\tilde{t}_w}{2} e^{i\delta_1} \begin{bmatrix} 1 \\ i \end{bmatrix} = \dfrac{(1+i)\tilde{t}_w}{2} e^{i\delta_1} \left|L\right\rangle & d > 0 \\ \\ \dfrac{(1-i)\tilde{t}_w}{2} e^{i\delta_1} \begin{bmatrix} 1 \\ -i \end{bmatrix} = \dfrac{(1-i)\tilde{t}_w}{2} e^{i\delta_1} \left|R\right\rangle & d < 0 \end{cases} . \tag{S6}$$

Equation (S6) describes the regulation of the circular polarization state of scattered light via paired apertures at different defocus positions ($d > 0$ or $d < 0$). When $d > 0$, the phase difference between the apertures is $\Delta\delta = \pi/2$, and the scattered light exhibits left-handed circular polarization ($\left|L\right\rangle$). When $d < 0$, $\Delta\delta = -\pi/2$ and the scattered light exhibits right-handed circular polarization ($\left|R\right\rangle$). The initial phase δ_1 determines the overall phase information of the scattered light. This equation reveals the mechanism for dynamically controlling the polarization state of scattered light by adjusting the defocus position, laying the foundation for the subsequent introduction of helical phase front.

S1.2 Propagation of scattered light via helical phase winding

For the introduction of helical phase front, the structure needs to exhibit the property of rotating around the propagation direction of the light. We arrange the paired apertures around the focal point at azimuth angle φ ,where $\theta = \pi/4 + \varphi$,and fixed lateral distance r_1 in series, the corresponding structure is illustrated in Fig.S2(a). Meanwhile, to ensure the circular polarization from each paired of apertures, radially polarized light incidence is used, the scattered light from each paired apertures in current x-y coordinate can be expressed as:

$$\left|E_{s\_each}\right\rangle = R(-\varphi)\left|E_{scat}\right\rangle = \begin{cases} \dfrac{(1+i)\tilde{t}_w}{2} e^{-i\varphi} e^{i\delta_1} \left|L\right\rangle & d > 0 \\ \dfrac{(1-i)\tilde{t}_w}{2} e^{i\varphi} e^{i\delta_1} \left|R\right\rangle & d < 0 \end{cases} . \tag{S7}$$

In addition, if the paired apertures are arranged in spiral curve with r_1 varies as:

$$r_1^2 = r_0^2 + m\frac{\varphi\lambda\left|d\right|}{n_g\pi} , \tag{S8}$$

where r_0 is the starting radius of the curve, and m is the arm number, with $m > 0$ for counterclockwise (CCW) spirals, and parameter s varies as described in equation (S4), the initial phase δ_1 is modulated correspondingly, enabling precise control of the phase evolution along the spiral. A corresponding structure with $m = 1$ is illustrated in Fig.S2(b), demonstrating the spatial arrangement. The distribution of the propagated scattered light under the above circumstances can be expressed as:

$$\left|E_{out}\right\rangle \sim \begin{cases} \displaystyle\int_{r_0}^{\sqrt{r_0^2 + m\frac{2\lambda\left|d\right|}{n_g}}} \int_0^{2\pi} \frac{(1+i)\tilde{t}_w}{2} e^{i\frac{n_g\pi}{d\lambda} r_0^2} \left|L\right\rangle e^{-i\varphi} e^{i(m\varphi\frac{\left|d\right|}{d})} e^{-i\frac{2\pi}{\lambda}\frac{\rho r\cos(\varphi_f - \varphi)}{z_f}} r\,d\varphi\,dr & d > 0 \\ \\ \displaystyle\int_{r_0}^{\sqrt{r_0^2 + m\frac{2\lambda\left|d\right|}{n_g}}} \int_0^{2\pi} \frac{(1-i)\tilde{t}_w}{2} e^{i\frac{n_g\pi}{d\lambda} r_0^2} \left|R\right\rangle e^{i\varphi} e^{i(m\varphi\frac{\left|d\right|}{d})} e^{-i\frac{2\pi}{\lambda}\frac{\rho r\cos(\varphi_f - \varphi)}{z_f}} r\,d\varphi\,dr & d < 0 \end{cases} , \tag{S9}$$

where (ρ, φ_f, z_f) are the observation point at observation plane as illustrated in Fig.S2(c), in addition, if the condition $z_f\lambda \gg \rho r_0, z_f\lambda \gg \rho r_1$ are satisfied, mathematically:

$$e^{-i\frac{2\pi}{\lambda}\frac{\rho r\cos(\varphi_f-\varphi)}{z_f}} \simeq \sum_{v=-\infty}^{\infty} J_v(-i\frac{2\pi r_0 \rho}{\lambda z_f}) i^v e^{iv(\varphi_f-\varphi)}, \tag{S10}$$

where J_v is the v^{th} Bessel function, thus equation (S9) can be simplified as:

$$|E_{out}\rangle \sim \begin{cases} J_{|m-1|} e^{i(m-1)\varphi_f} |L\rangle & d>0 \\ J_{|1-m|} e^{i(1-m)\varphi_f} |R\rangle & d<0 \end{cases}. \tag{S11}$$

Therefore, by adjusting the positions of the structure with relative to the focus and arm number of the spiral, we can flexibly control the handedness of circular polarization and helical phase winding of the scattered light, which are also referred as SAM and OAM states of the scattered light. Fig.S2(d) schematically illustrates the output light beam when the structure is positioned at $d > 0$ defocus position, with radially polarized light incidence. By adjusting m to +1, 0, and -1, the scattered light is locked to LCP, while generating different OAM topological charge: $\ell_{out} = 0, -1, \text{and} -2$.

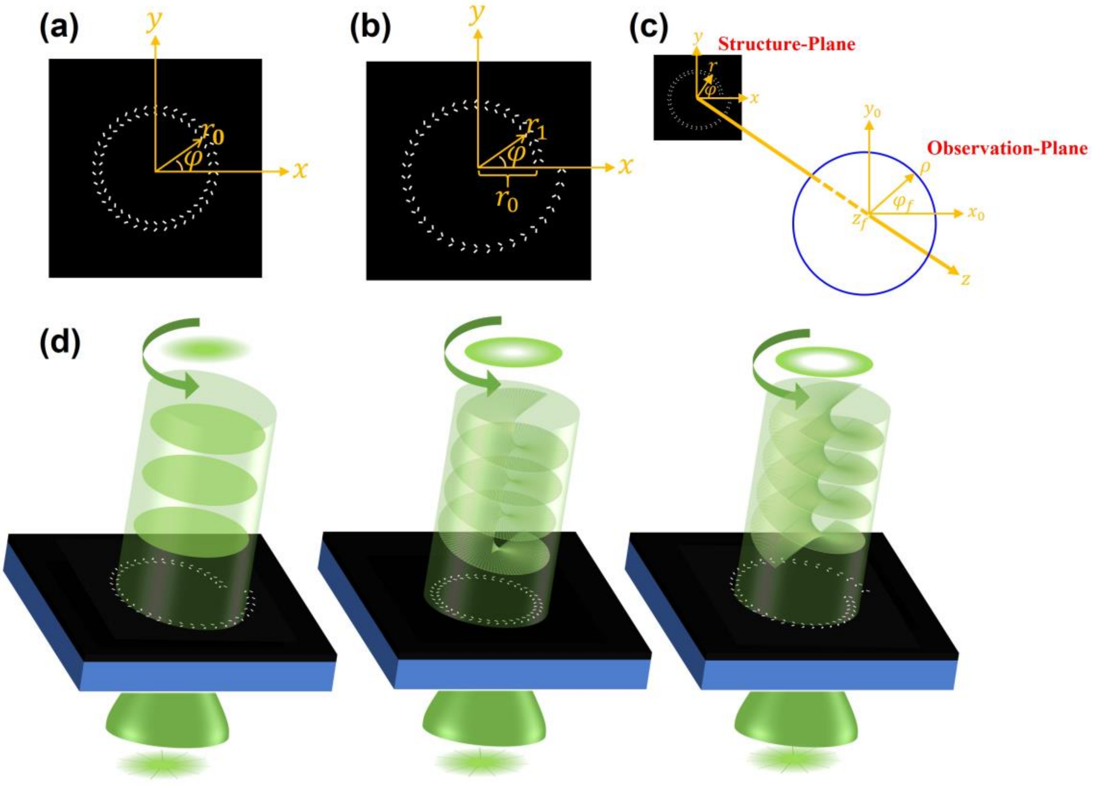

Fig.S2: (a) Paired apertures arranged at azimuth angle φ and fixed lateral distance r_1 in series. (b) Paired apertures arranged in spiral curve with an arm number m=1. (c) Schematic of the coordinate system, showing the structure plane and observation plane. (d) Schematic showing the modulation of scattered light at defocus positions where $d > 0$. Adjusting the arm number m to $+1, 0, \text{and} -1$ locks the scattered light to LCP with different OAM topological charge: $\ell_{out} = 0, -1 \text{ and } -2$.

S2、Purity of circular polarization (PCP) of the scattered light

In order to determine the polarization properties of the scattered light, we define the purity of circular polarization (PCP) as:

$$PCP = \frac{I_{LCP}(k_x,k_y) - I_{RCP}(k_x,k_y)}{I_{LCP}(k_x,k_y) + I_{RCP}(k_x,k_y)} = \frac{E_{LCP}(k_x,k_y)E_{LCP}(k_x,k_y)^* - E_{RCP}(k_x,k_y)E_{RCP}(k_x,k_y)^*}{E_{LCP}(k_x,k_y)E_{LCP}(k_x,k_y)^* + E_{RCP}(k_x,k_y)E_{RCP}(k_x,k_y)^*},$$

$$\begin{aligned} E_{LCP}(k_x,k_y) &= \langle L \mid E_f \rangle = E_{fx}(k_x,k_y) - iE_{fy}(k_x,k_y) \\ E_{RCP}(k_x,k_y) &= \langle R \mid E_f \rangle = E_{fx}(k_x,k_y) + iE_{fy}(k_x,k_y) \end{aligned}, \tag{S12}$$

where $E_{fx}(k_x,k_y), E_{fy}(k_x,k_y)$ is the electric field component in the observation plane. Furthermore, in Fig.2 of the main text, we have shown that the *PCP* fluctuate with the change of apertures' spacing s and lateral distance r_1, which results it varies in -1<*PCP* <1, therefore the equation (S11) can be further modified as:

$$|E_{out}\rangle \sim \begin{cases} \eta_{1\_+d} J_{|m+1|} e^{i(m+1)\varphi} |R\rangle + \eta_{2\_+d} J_{|m-1|} e^{i(m-1)\varphi} \; |L\rangle & d>0 \\ \\ \eta_{1\_-d} J_{|1-m|} e^{i(1-m)\varphi} |R\rangle + \eta_{2\_-d} J_{|m+1|} e^{-i(m+1)\varphi} \; |L\rangle & d<0 \end{cases}, \tag{S13}$$

where $\eta_{1\_+d}, \eta_{2\_+d}, \eta_{1\_-d}, \eta_{2\_-d}$ are amplitude coefficients of different circular polarization at different defocusing positions. From the above expression, we can see that although imperfect polarization transition result in mixing of LCP and RCP in the observation plane, these two different circular polarizations are appended with different phase winding numbers and forms different field distribution. In order to characterize the overlap of those polarizations, we define the overlap factor:

$$Overlap = \frac{\left[\iint |E_{LCP}(k_x,k_y)| \bullet |E_{RCP}(k_x,k_y)| \, dk_x dk_y \right]^2}{\iint |E_{LCP}(k_x,k_y)|^2 \, dk_x dk_y \bullet \iint |E_{RCP}(k_x,k_y)|^2 \, dk_x dk_y}, \tag{S14}$$

S3、Analysis of the energy conversion efficiency

Due to the subwavelength dimensions of the nano-apertures array, the overall transmission efficiency of the system is relatively low. Specifically, the high reflectivity and absorptive properties of the silver film further reduce the light utilization. As shown in Table S1, the average transmission conversion efficiency under different defocus states (*d>0* and *d<0*) is less than 0.126%. We also observe variations in transmission efficiency for different structural arrangement (m=+1,m=0,m=−1), which are attributed to differences in the coupling efficiency between the incident light and the structure, as well as the transmission characteristics of various modes. To further improve the efficiency, future work could focus on optimizing the geometric design and material properties of the nano-apertures. For instance, increasing the number of slits, adjusting their width, depth, and arrangement.

Table S1. Conversion Efficiency

Arm number	Defocus	Efficiency
$m = +1$	$d > 0$	0.096%
	$d < 0$	0.099%
$m = 0$	$d > 0$	0.124%
	$d < 0$	0.126%
$m = -1$	$d > 0$	0.096%
	$d < 0$	0.097%

S4、Preparation of structures

The structures are prepared by focused ion beam etch processes with precise alignment and the main steps are shown in Fig.S3. First, the BK7 Silica substrate is cleaned by acetone and ethyl alcohol to remove impurities and organic matter. The quantum dot microspheres are fully diluted and spin-coated onto the substrate. Then, 200nm Ag film is deposited by e-beam evaporator (PVD75 Proline), the Uv resist(S1828) is spin-coated onto the Ag film and patterned with cross marks by an optical aligner (MABA6 Gen4). The pattern is then transferred to Ag film with a reactive ion etching process (PlasmaPro NGP 80), the remaining photoresist is removed by acetone. The position of the microsphere relative to the markers is confirmed by photoluminescence imaging, and the method can be found in Ref[4]. Finally, the ring geometry paired apertures are patterned around the microsphere by focused ion beam etch (Orion Nanofab).

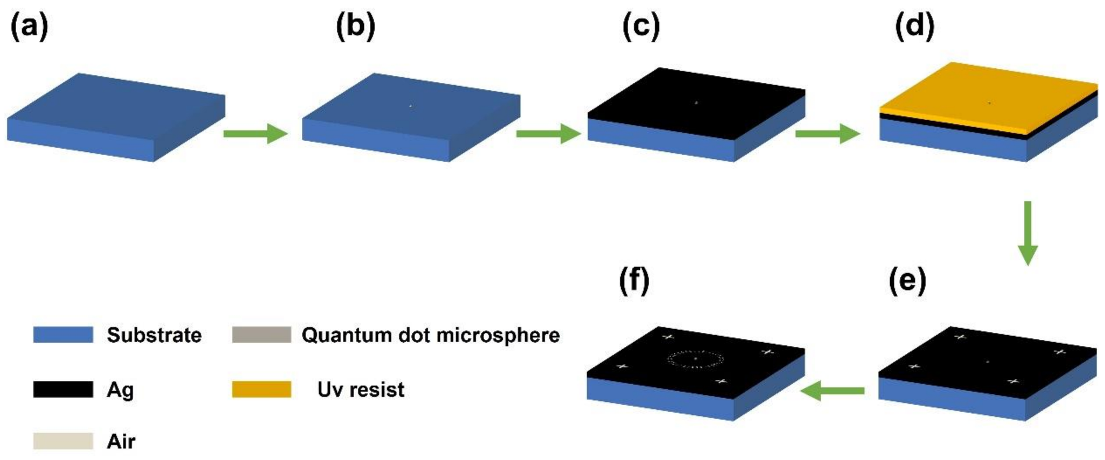

Fig. S3: Structure preparation process. (a) Silica substrate cleaning. (b) Spin coating quantum dot microspheres. (c) Deposition of 200 nm Ag on the silicon substrate. (d) Spin coating Uv resist and lithography. (e) Reactive ion etching to transfer marks into Ag film and removing of photoresist. (f) Spiral apertures array fabrication using focused ion beam etch.

S5、Experimental setup

After the laser with wavelength of 532nm is expanded, it is converted into radially polarized light by a linear polarizer (LP) and radial polarization converter (RPC), and then focused to the center of the structure by objective lens (100X, N.A.=1.49, Olympus). The polarization state of the scattered light is controlled by adjusting the position of the structure relative to the focus. Meanwhile, a collecting objective lens (20X, N.A.=0.75, Olympus) is placed above the structure to collect scattered light from the structure, a quarter wave plate(QWP) and a LP are inserted in the collection path to project the scattered light into different circular polarization state. The fast axis of QWP is set to 45°(-45°), while the LP is placed vertically, which correspond to the RCP(LCP) projection, The result is imaged to a CCD camera (INFINITY2-5, LUMENERA) through lens, and corresponding experimental setup is shown in Fig.S4.

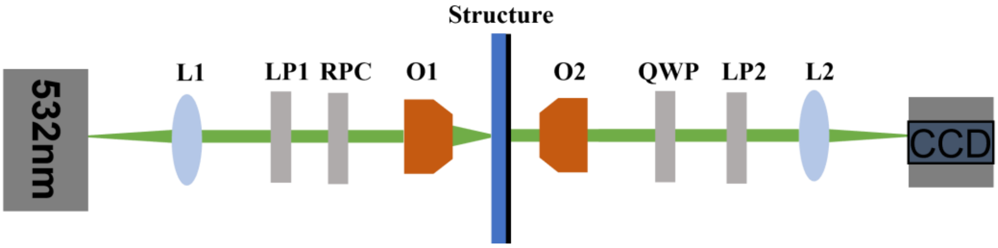

Fig. S4: Optical setup for measuring scattered light’s polarization states, L lens, LP polarizer, RPC radial polarization converter, O1 objective (100x, N.A.=1.49), O2 objective (20x, N.A.=0.75), QWP quarter-wave plate.

For determination of the scattered light’s OAM topological charge, we use self-interference method, where the number and direction of the interference forked fringes indicating the sign and magnitude of OAM topological charge [5]. This commonly used method splits the scattered light into two beams (50:50), which then arrive at the observation plane simultaneously. The interference fringes with different OAM topological charge and plane wave are shown in Fig.S4. When the sign of OAM topological charge is reversed, the direction of the forked fringes are also reversed, and the number of forked fringes increases with the magnitude of the OAM topological charge.

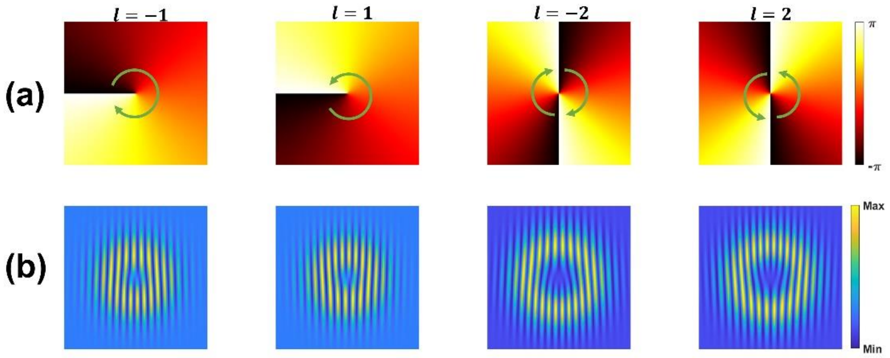

Fig. S5： Analytically calculated (a) phase profiles with different OAM topological charge (b) interference patterns with plane wave.

The corresponding setup is shown in Fig.S6, where an interferometer is modified by incorporating a small tilt in the beam by rotating the mirror M2. Rotating the mirror by angles α and β introduces a tilt in the beam propagation direction along x and y axes, respectively, so that the dark center of one doughnut overlaps with the bright ring of the other beam.

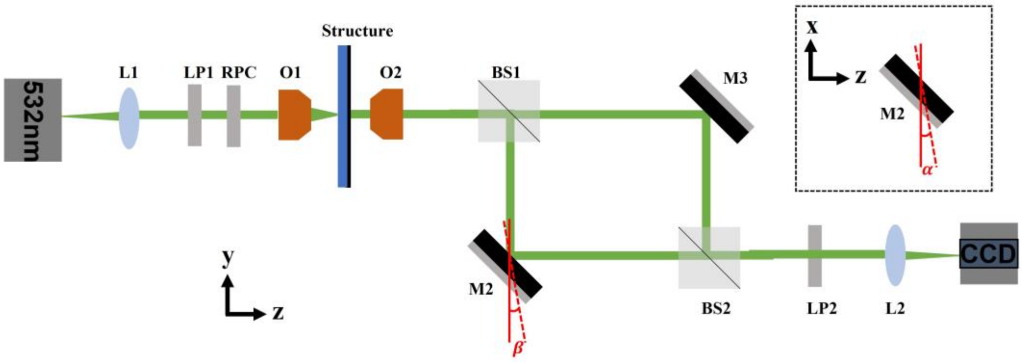

Fig. S6: Optical setup for self-interference measurements of the OAM topological charge. LP linear polarizer, RPC radial polarization converter, O1 objective (100x, N.A.=1.49), O2 objective (20x, N.A.=0.75), BS beam splitter (50:50), M mirror.

References

1. T. Zang, H. Zang, Z. Xi et al., "Asymmetric Excitation of Surface Plasmon Polaritons via Paired Slot Antennas for Angstrom Displacement Sensing," Physical Review Letters 124, 243901 (2020).
2. M. Khorasaninejad, and K. B. Crozier, "Silicon nanofin grating as a miniature chirality-distinguishing beam-splitter," Nature Communications 5, 5386 (2014).
3. J. W. Goodman, Introduction to Fourier optics (Roberts and Company publishers, 2005).
4. S. Liu, K. Srinivasan, and J. Liu, "Nanoscale Positioning Approaches for Integrating Single Solid‐State Quantum Emitters with Photonic Nanostructures," Laser & Photonics Reviews 15 (2021).
5. C. Huang, C. Zhang, S. Xiao et al., "Ultrafast control of vortex microlasers," Science 367, 1018-1021 (2020).